



World Hydrogen Energy Conference 2012

Amorphous TiO₂ as a photocatalyst for hydrogen production: a DFT study of structural and electronic properties

Kulbir Kaur^a and Chandra Veer Singh^{a,*}

^a*Department of Material Science and Engineering, University of Toronto, 184 College St. Suite 140, Toronto, Ontario M5S 3E4 Canada.*

Abstract

In recent years, photocatalytic splitting of water to produce hydrogen has attracted significant attention. Crystalline forms of titanium dioxide (TiO₂) have been investigated for decades. Amorphous TiO₂, although less expensive, has not been studied as thoroughly. This study investigates the structural and electronic properties of amorphous TiO₂. Molecular dynamics simulations are used to prepare multiple amorphous TiO₂ samples having different number of atoms. The structural analysis agrees well with the experimental data. Electronic properties of amorphous TiO₂ are investigated through density functional theory calculations. Band gap characteristics of amorphous TiO₂ are compared with experimental data for amorphous as well as crystalline (rutile and anatase) TiO₂ phases. Analysis of electronic properties suggests that amorphous TiO₂ may prove as a cheaper, more abundant, but somewhat less efficient photocatalyst as compared to crystalline TiO₂.

© 2012 The Authors. Published by Elsevier Ltd.

Selection and/or peer-review under responsibility of Canadian Hydrogen and Fuel Cell Association

Keywords: Hydrogen production ; Photocatalysis; Amorphous TiO₂; Structural properties; Electronic properties.

1. Introduction

Titanium dioxide (TiO₂) is a safe, abundant and inexpensive photocatalytic material. It has therefore attracted wide attention in recent years for photocatalytic splitting of water [1,2], water decontamination [3] and solar cells [4]. Most of the efforts so far have been focused on improving the photocatalytic properties of the crystalline phases only, as the amorphous TiO₂ structure is reported not as good photoactive substance due to its broad band gap and disorder [5]. However, amorphous TiO₂ (aTiO₂) has a larger surface area which leads to higher adsorptivity. It is also more widely available in nature and can be prepared at room temperature. Furthermore, it is easier to process into different forms and may allow

* Corresponding author. Tel.: +1-416-946-5211; fax: +1-416-978-4155.
E-mail address: chandraveer.singh@utoronto.ca (Chandra Veer Singh)

much wider range of dopants. These useful characteristics have led to recent attention to exploring aTiO₂ as an alternative to crystalline TiO₂. Quite recently, aTiO₂ dye sensitized solar cell has been found to exhibit higher efficiency as compared to the nano-crystalline TiO₂ layer [6]. Buddee et al. [7] have reported that Fe/Cr doped aTiO₂ showed enhanced photo catalytic activity under both UV & visible light and these can also be used endlessly without any changes, indicating another significant advantage of aTiO₂ over crystalline forms. More recently, Chen et al. [8] have prepared disorder engineered TiO₂ nanocrystals and found that mid gap states arising out of structural disorder upshift the valence band edge effectively reducing the band gap and increasing its photocatalytic efficiency. The analysis of structural properties of aTiO₂ nanoparticles has been conducted using MD [9].

In view of above reports, it is therefore necessary to understand the atomic level structure of aTiO₂, its electronic properties in more depth; and explore its potential as a cost-effective photocatalyst for large-scale hydrogen production through sunlight-enabled water splitting. The structural and electronic properties of aTiO₂ have also been investigated recently by Prasai et al [10]. In the present study we analyze the structural disorder and electronic properties of aTiO₂ in a similar way through density functional theory (DFT) calculations; however our sample preparation and some results are different from the cited study, as will be discussed later in the paper. The defects in aTiO₂ and the localized states in the band gap corresponding to the structural defects are identified. As amorphous semi-conductors are difficult to model due to lack of periodicity and the complexity of structural details at the atomistic level, we propose atomistic aTiO₂ models formed by molecular dynamics (MD). Multiple aTiO₂ samples having different number of atoms and using different heating and quenching rates are also investigated. To confirm the amorphicity of the models, structural properties are compared to experimental data. Finally, electronic properties of aTiO₂ calculated using DFT are compared with the crystalline phases.

2. Computational details

2.1 Sample preparation methodology

Three model samples of bulk aTiO₂ with supercell dimensions of $2 \times 2 \times 3$ (72 atoms); $2 \times 2 \times 4$ (96 atoms) and $3 \times 3 \times 4$ (216 atoms) were prepared using molecular dynamics (MD) simulations. Initial configuration was chosen with a side length obtained by rescaling crystalline configuration of rutile (tetragonal, space group p42/mnm) so as to have density equal to aTiO₂, i.e. 3.8 gcm^{-3} , with lattice parameters $a = b = 4.761 \text{ \AA}$, $c = 3.066 \text{ \AA}$ and $u = 0.305$. Matsui-Akaogi (MA) force field [11] was used for short range interactions; and the affect of long range Coulomb interactions were taken into account using damped shifted force Coulomb sum method. MD simulations were carried out using DLPOLY [12]. Periodic boundary conditions were used. Each sample was first subjected to geometric optimization in micro canonical ensemble (NVE) by ‘zero’ temperature MD. To eliminate the memory of initial structure, all the crystalline samples were first heated up to temperature greater than the melting point of rutile, as performed by Rino et. al [13]. Thereafter the sequential heating and quenching were performed. After every heating and quenching, samples were equilibrated for sufficiently long time to assure that they attain the steady state configurations, with a simulation time step of 1 fs. After quenching the samples to the room temperature followed by equilibration, they were finally relaxed to 0 K to attain ground state.

The above sample preparation process can sometimes lead to dangling bonds which can cause erroneous band gap levels, see e.g. [14]. Therefore, careful checks were performed periodically to make sure that no atom should remain unbonded creating dangling bonds. The structures of prepared samples are presented in Figs. 1 (a)-(c), respectively. Final samples obtained from MD at 0K temperature were further relaxed using DFT calculations before calculating there structural and electronic properties. Details of the ab-initio calculations are provided below.

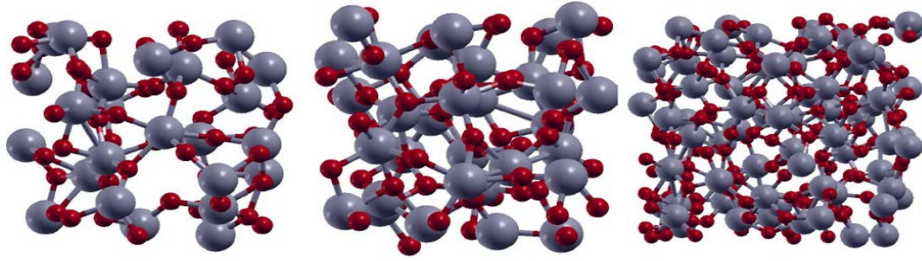


Figure 1. The structure of 72-atom (left), 96-atom (middle) and 216-atom (right) models of amorphous TiO_2 . The red and grey spheres represent O and Ti atoms respectively.

2.2 *Ab-initio calculations of electronic properties*

DFT calculations were performed using Quantum Espresso [15] software package to investigate the electronic characteristics of aTiO₂ samples. The interaction between the valence electrons and the ionic core is described by the generalized gradient approximation (GGA) in the Perdew-Burke-Erzerhof (PBE) formulation [16] and Vanderbilt ultrasoft pseudo-potentials [17]. The wave functions were expanded with kinetic energy cutoffs of 40 Ry and 400 Ry for the smooth part of the electronic wave functions and augmented electron density, respectively. The Monkhorst-Pack grid [18] with $2 \times 2 \times 3$, $2 \times 2 \times 3$ and $1 \times 1 \times 2$ k points was used in SCF iterations and $4 \times 4 \times 6$, $4 \times 4 \times 6$ and $2 \times 2 \times 4$ k points was used for electronic density of states (DOS) computation for 72-atom, 96-atom and 216-atom model respectively. These values were chosen after full convergence studies. All calculations were spin polarized. The atomic structures were relaxed using the conjugate gradient minimization algorithm, until the magnitude of residual Hellman-Feynman force on each atom was less than 10^{-3} Ry/Bohr. Before electronic properties calculations all the samples were relaxed at zero pressure by variable cell relaxation. In order to enable direct comparison of amorphous TiO_2 with crystalline phases, rutile and anatase structures were also investigated. The bulk lattice parameters for zero pressure crystalline TiO_2 obtained by variable cell relaxation using DFT were in reasonable agreement with experimental data. For instance, for rutile $a = b = 4.6155 \text{ \AA}$ and $c = 2.96 \text{ \AA}$, which agree with experiments [19–22] as well as with other theoretical calculations [23–26].

3. Results and discussion

3.1 *Structural Properties*

Before calculating electronic properties of amorphous samples, their structural properties were calculated and compared with experimental data to ensure the amorphicity of the model aTiO₂ samples. Specifically, partial pair correlation functions (PPCFs), coordination numbers (CNs), bond length, bond angle and dihedral angle distributions were studied. Two-body correlations were determined by PPCF, $g_{\alpha\beta}(r)$, which is defined as

$$\langle n_{\alpha\beta}(r) \rangle \Delta r = 4\pi r^2 \rho c_{\beta} g_{\alpha\beta}(r) \Delta r \quad (1)$$

where $\langle n_{\alpha\beta}(r) \rangle \Delta r$ is the number of β particles in the shell of inner radii r and thickness Δr , around particle α . The angular brackets denote the ensemble average as well as the average over all the α 's. The number density $\rho = N/\Omega$, with $N = N_{\text{Ti}} + N_{\text{O}}$ and Ω is the volume of the system, $c_{\beta} = N_{\beta}/N$ is the concentration of β particles and N_{β} is their total number. The calculated PPCFs for Ti-Ti, Ti-O and O-O pairs for the three aTiO₂ models along with experimental data [27] are shown in Fig. 2. The calculated PPCFs agree reasonably well with experimental data for sputtered TiO₂ amorphous layers [27], and as expected, the larger samples correlate better with the reported experimental data. The peak positions in

the figure correspond to the nearest neighbour (NN) distances, and are calculated as 3.1 Å and 3.4 Å for the 72-atom model, 3.0 Å and 3.6 Å for the 96-atom model and 3.13 Å and 3.53 Å for the 216-atom model. They are also in close agreement with experiments reported by Petkov et al. [27], who found 1st and 2nd nearest neighbor peaks corresponding to edge-sharing and corner-sharing Ti-Ti pairs at 3.0 Å and 3.55 Å, respectively. The calculated Ti-O and O-O 1st NN distances are at 1.9 Å and 2.8 Å for 72-atom model, 1.9 Å and 2.7 Å for 96-atom model and 1.92 Å and 2.7 Å for 216-atom model, also in reasonable agreement with the experimental values of 1.96 Å and 2.67 Å respectively.

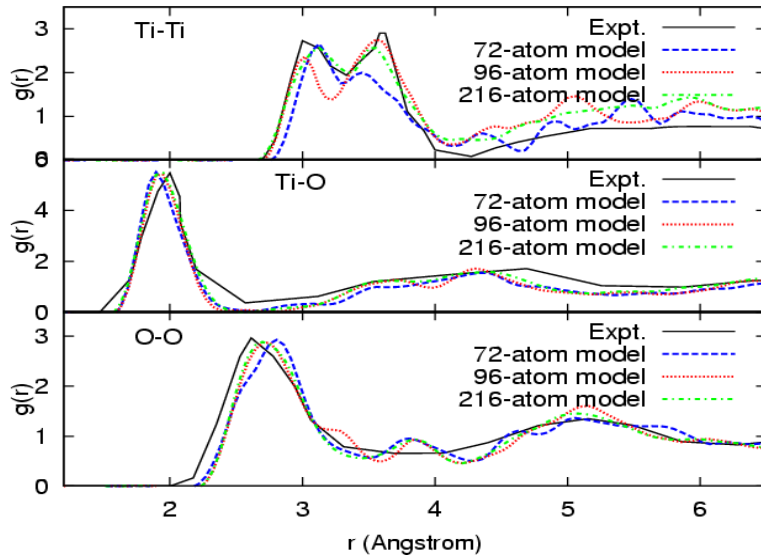


Figure 2. Ti-Ti, Ti-O and O-O partial pair correlation functions (PPCFs) for 72-atom, 96-atom and 216-atom aTiO₂ model along with experimental data [27].

The distribution of coordination numbers (CNs) $Z_{\text{Ti-O}}$, of Ti and $Z_{\text{O-Ti}}$, of O atoms were determined by counting the number of O and Ti atoms respectively, within the range of first minima of $g_{\text{Ti-O}}(r)$ throughout the sample. This minima is found to be 2.85 Å for 72-atom, 96-atom and 216-atom aTiO₂ models. CN of Ti is 6 and O is 3 for crystalline bulk rutile but for amorphous TiO₂ samples Ti atoms have the CNs 1, 2, 3, 4 and 5 in addition to 6 and O atoms have CNs 1, 2, 4 and 5 in addition to 3. The relative percentages of CNs for amorphous phase are tabulated in Table 1. The average CN of Ti is 4.125, 4.406 and 4.736 for 72-atom, 96-atom and 216-atom models, respectively. On the other hand, the average CN of O is 2.104, 2.625 and 2.632 for 72-atom, 96-atom model and 216-atom models, respectively. The corresponding experimental CNs for Ti and O are $5.6 \pm 10\%$ and $2.8 \pm 10\%$ respectively [27]. Above analysis shows that CN of all aTiO₂ samples is in agreement with the experimental data. It can be noted from table 1 that most of the Ti and O atoms of amorphous samples tend to remain 6-fold and 3-fold respectively. The larger 216-atom model behaves more like a bulk system and hence agrees more closely with experimental results [27], which were also for the bulk amorphous system. These results are qualitatively similar to those presented by Prasai et al. [10], who used a different force field characterization in preparing amorphous samples, suggesting relative consistency in structural properties.

The analysis of bond length distribution for amorphous models shows that most of Ti-O bond lengths get distributed between 1.86 to 2.1 Å for all the three amorphous samples, whereas for crystalline rutile Ti-O bond lengths are at 2.017 and 2.05 Å. Our results agree well with the experimental results of Manzini et. al. [28], who found two Ti-O separations of 1.79 and 1.93 Å in amorphous sol-gel TiO₂. It is

Table 1: Relative percentages of Ti and O atoms with coordination numbers (CNs) $Z_{\text{Ti-O}} = 1, 2, 3, 4, 5,$ and 6 and $Z_{\text{O-Ti}} = 1, 2, 3, 4$ and 5 for amorphous TiO_2 models.

CN	72-atom model	96-atom model	216-atom model
		$Z_{\text{Ti-O}}$	
1	4.17	3.13	2.78
2	12.5	3.13	8.33
3	25.00	21.88	12.50
4	8.33	28.13	12.50
5	25.00	9.38	20.83
6	25.83	34.38	40.28
		$Z_{\text{O-Ti}}$	
1	10.42	12.50	12.50
2	62.50	10.94	18.056
3	14.58	65.63	56.25
4	0.00	7.81	6.25
5	6.25	0.00	4.167

noted that large number of Ti-O bonds get compressed and few get expanded as compared to crystalline phase of TiO_2 . Bond angle analysis of the amorphous models shows that in the amorphous phase bond angles get dispersed from 55° to 157° although majority of bond angles are between 70° to 110° . Rino et al. [13] also found the main peak at 90° . The dihedral angles in all the amorphous models show no peaked structure and are nearly uniformly distributed between 0° and 360° . Thus, expectedly the planar orientation becomes nearly random for amorphous samples.

3.2 Electronic properties

To describe the electronic structure of amorphous TiO_2 the electronic density of states (DOS) and the inverse participation ratio (IPR) were analyzed. The total DOS for all the three model of aTiO_2 along with that crystalline rutile of supercell size $2 \times 2 \times 3$ (72 atoms) and anatase of supercell size $2 \times 2 \times 2$ (48 atoms) using DFT are shown in Fig. 3. To understand the electronic properties in further detail the atomic partial density of states (PDOS) for the d electrons of Ti atom and p electrons of O atoms were investigated for all the samples. As DOS of all the amorphous models have similar characters with slight differences in detail, we have shown PDOS for the 96-atom model only (see Fig. 4). Only the valence band (VB) and conduction band (CB) are shown in the figures. The spin-up and spin-down contributions are displayed as top and bottom, respectively, in Fig. 4. The zero energy value is set at the top of the valence band to analyze the relative change in the band with more clarity. The Fermi energy is represented by the vertical line in the band gap. DOS and PDOS graphs show that VB and CB mainly consists of O p and Ti d orbitals respectively. Thus, high localization obtained in VB and CB tails (shown by IPR analysis, Fig. 5) is on O p and Ti d orbitals respectively. The band gap is measured as difference between highest and lowest occupied molecular orbitals (HOMO-LUMO gap) based on the Γ point in the k -space, as is usually done for crystalline systems. To further understand CB and VB tails, detailed IPR analysis is performed.

The band gap of amorphous models can also be determined by analyzing the change of the localization degree of the electronic states near the VB and CB edges. The localization of each electronic state was quantified here by analyzing the inverse participation ratio in aTiO_2 .

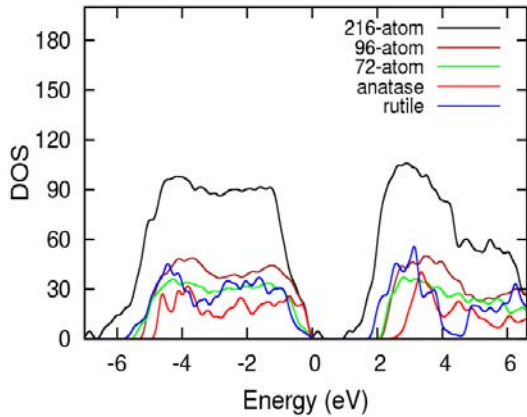


Figure 3. Comparison of total density of states for crystalline (rutile and anatase) and amorphous (72-atom, 96-atom and 216-atom models) TiO₂ structures using DFT.

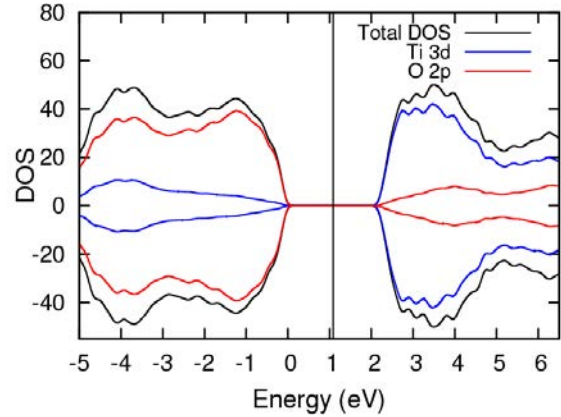


Figure 4. The density of states projected on the p and d orbitals along with the total density of states for the 96-atom model of amorphous TiO₂ using DFT.

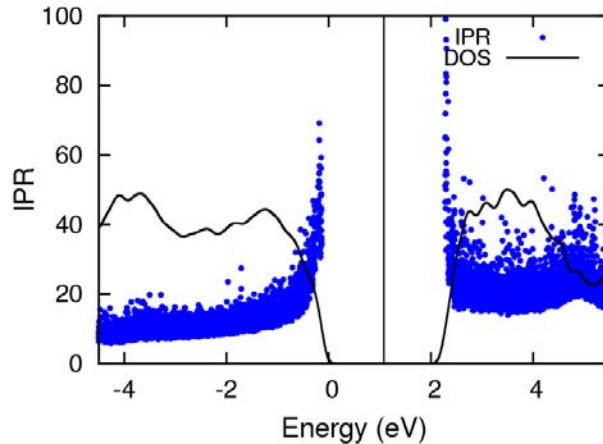


Figure 5. Plot of inverse participation ratio (IPR) for the 96-atom model of aTiO₂. Large IPR implies strong localization.

The IPR of an orbital $\psi_n(\vec{r}_i)$, $I(\psi_n)$, is defined as

$$I(\psi_n) = N \frac{\sum_{i=1}^N |\psi_n(\vec{r}_i)|^4}{[\sum_{i=1}^N |\psi_n(\vec{r}_i)|^2]^2}, \quad (2)$$

where N is the number of volume elements in the cell and i is the index of the volume element. The IPR is large for highly localized states and small for delocalized states. Ideally, a localized orbital presents $I(\psi) = N$, whereas a delocalized orbital presents $I(\psi) = 1$. Thus IPR can identify a level as belonging to the band (delocalized), to the band tail (partially localized), or to the band gap (highly localized).

The plot of IPR and total DOS for the 96-atom aTiO₂ model is depicted in Fig. 5. The bottom of the CB and the top of the VB was determined as the energy where the IPR becomes higher than the average IPR of those levels sitting a few electron volts below the VB top. The mobility gap, defined as the gap between extended valence and conduction states, is estimated as $E_g = 2.85$ eV for the 72-atom and 96-atom model and 2.7 eV for the 216-atom model. As a comparison with crystalline TiO₂, we obtained a

band gap of 1.78 eV for rutile and 2.53 eV for anatase TiO₂. Experimental values of band gap for rutile and anatase are 3.03 eV [21] and 3.20 eV [35], respectively. While DOS graphs are similar to Prasai et al. [10], band gap values in present study are closer to the experiments. Relatively larger band gap of aTiO₂ with respect to rutile and anatase, and the presence of band tail states suggest that it is photocatalytically less efficient than the crystalline forms. Since there is a large number of levels with different IPR's in the top of the VB, there is some uncertainty in defining the gap. Also as the dimensions of simulation cells considered here are small relative to the bulk amorphous material, the results are expected to improve with increasing model sizes. Finally, it is noted that we used finite cells with periodic boundary conditions. Hence, it is possible that the levels which are in the band tails near the energy-band edges may present some fictitious delocalization. A more detailed investigation on the band tail properties of aTiO₂ with very large simulation cells of a few thousand atoms [36] should be carried out in future studies.

4. Summary

In summary, we have investigated structural and electronic properties of amorphous TiO₂ with the hope that it may prove as prospective candidate for use in hydrogen production using photocatalytic water splitting technique. Classical molecular dynamics with a two body inter-atomic potential was utilized to prepare amorphous TiO₂ structure via “melt-and-quench” method. To investigate effect of different number of atoms and different heating and quenching rates, three different samples were prepared. The analysis of radial distribution function, coordination number, bond length, bond angle and dihedral angle distributions suggested very good agreement of aTiO₂ structural properties with available experimental data, confirming the appropriate amorphicity of these samples. Density functional theory was used further to study electronic properties of amorphous TiO₂ samples. Band gap of amorphous TiO₂ samples having different number of atoms and prepared with different heating and quenching rates are compared with experimental band gap of amorphous as well as crystalline (rutile and anatase) TiO₂. The calculated structural properties are also qualitatively similar to ref. [10] with samples prepared using a different force field characterization; however, the band gap observed in present calculations is much closer to the experimental data. The spatial localization of all the energy levels has been identified by analyzing the inverse participation ratio. From IPR analysis it was found that band-tail states near the band edges are localized in amorphous TiO₂ in contrast to the crystalline TiO₂ due to the presence of bond angle disorder. The valence and conduction tail states result from the positional disorder of O and Ti atoms, respectively. The extent of tailing depends on disorder present. Higher the disorder is more the overlapping of bands in the band gap. The electronic density of states and electronic localization, were found to be quite insensitive to the variation in local disorder among different sized models. The analysis of the electronic properties suggests that the electronic structure of aTiO₂ is similar to that of crystalline electronic structure, but with a larger band gap. This provides hope that amorphous form of TiO₂ may prove as a cheaper and more abundant alternative to crystalline forms. However, to fully realize the potential of aTiO₂ as a cost-effective photocatalyst, a more detailed investigation on the nature of band tail states, using larger simulation cells, and doping with suitable elements need to be carried out. These in-depth studies on the role of disorder and dopant nature on electronic properties of aTiO₂ are currently being performed and will be reported in future.

Acknowledgements

Computations were performed on the HPC supercomputer at the SciNet HPC Consortium [37]. SciNet is funded by: the Canada Foundation for Innovation under the auspices of Compute Canada; the Government of Ontario; Ontario Research Fund - Research Excellence; and the University of Toronto. The authors gratefully acknowledge their support.

References

- [1] Fujishima A, Zhang X, Tryk Donald A. TiO₂ photocatalysis and related surface phenomena. *Surface Science Reports* 2008; **63**:515–582.
- [2] Ni M, Leung M K H, Leung D Y C, and Sumathy K. A review and recent developments in photocatalytic water-splitting using TiO₂ for hydrogen production. *Renewable & Sustainable Energy Reviews* 2007; **11** :401.
- [3] Ollis D F, Al-Ekabi H. Photocatalytic purification and treatment of water and air. *Elsevier: Amsterdam, The Netherlands* 1993.
- [4] Wang Y Q, Chen S G, Tang X H, Palchik O, Zaban A, Kolytyn Y, Gedanken A. Mesoporous titanium dioxide: sonochemical synthesis and application in dye-sensitized solar cells. *J. Mater. Chem.* 2001; **11**:521.
- [5] Rahman M, MacElroy D, Dowling D P. Influence of the physical, structural and chemical properties on the photoresponse property of magnetron sputtered TiO₂ for the application of water splitting. *J Nanoscience and Nanotechnology*, 2011; **11**, 8642.
- [6] Han C H, Lee H S, Lee K W, Han S D, Singh I. Synthesis of amorphous er₃₊-yb₃₊ co-doped tio(2) and its application as a scattering layer for dye-sensitized solar cells. *Bull. Korean Chem. Soc.* 2009, **30**:219.
- [7] Budee S, Wongnawa S, Sirimahachai U, Puetpaibool, W. Recyclable UV and visible light photocatalytically active amorphous TiO₂ doped with M (III) ions (M = Cr and Fe), *Mater Chem Phys* 2011, **126**:167.
- [8] Xiaobo Chen, et al. Increasing solar absorption for photocatalysis with black hydrogenated titanium dioxide nanocrystals. *Science* 2011; **331**:746.
- [9] Hoang VV, Zung H, and Trong NHB. Structural properties of amorphous TiO₂ nanoparticles, *Euro Phys D* 2007, **44**:515.
- [10] Prasai B et al. Properties of amorphous and crystalline titanium dioxide from first principles. *J Mater Sci* 2012; **47**: 7515-7521.
- [11] Matsui M, Akaogi M. Molecular Dynamics simulation of the structural and physical properties of the four polymorphs of TiO₂. *Molecular Simulations* 1991; **6**:239.
- [12] Smith W, Todorov I T. A short description of DL_POLY. *Molecular Simulations* 2006; **32**:935.
- [13] Rino J P, Studart N. Structural correlations in titanium dioxide. *Phys. Rev. B* 1999; **59**:6643.
- [14] Cai B, Drabold D A. Properties of amorphous GaN from first-principles simulations. *Phys. Rev. B*, 2011; **84**: 075216.
- [15] Giannozzi P, Baroni S, Bonini N, Calandra M, Car R, Cavazzoni C, Ceresoli D, Chiarotti G L, Cococcioni M, Dabo I, et al. Quantum espresso: a modular and open-source software project for quantum simulations of materials. *Journal of Physics: Condensed Matter* 2009; **21**:395502.
- [16] Perdew J P, Burke K, Ernzerhof M. Generalized gradient approximation made simple. *Phys. Rev. Lett.* 1996; **77**:3865.
- [17] Vanderbilt D. Soft self-consistent pseudopotentials in a generalized eigenvalue formalism. *Phys. Rev. B* 1990, **41**:7892.
- [18] Monkhorst H J and Pack J D. Special points for brillouin-zone integrations. *Phys. Rev. B* 1976, **13**:5188.
- [19] Wyckoff R W G. *Crystal structures. John wiley and Sons, Inc. New York, London* 1963; 1.
- [20] Inorganic crystal structure database (icsd). *NIST Release* 2010.
- [21] Amtout A and Leonelli R. Optical properties of rutile near its fundamental band gap. *Phys. Rev. B* 1995, **51**:6842.
- [22] Lide D R. CRC Handbook of Chemistry and Physics, 77th ed. Raton Boca, 1997.
- [23] Song Q T, Yang P, Wang J B. *J. Mater. Sci. Eng.* 2008; **26**:435.
- [24] Changyol L, Philippe G, Xavier G. Lattice dynamics and dielectric properties of incipient ferroelectric TiO₂ rutile. *Phys. Rev. B* 1994; **50**:13379.
- [25] Zeng Z L, Zheng G, Wang X C, He K H, Chen Q L, Yu L, Wang Q B. First-principles study on the structural and electronic properties of double n atoms doped-rutile TiO₂. *J. Atomic and Molecular Sciences* 2010; **1**:177.
- [26] Shao G. Electronic structures of manganese-doped rutile TiO₂ from first principles. *J. Phys. Chem. C* 2008; **112**:18677.
- [27] Petkov V, Holzhuter G, Tronge U, Gerber Th, Himmel B. *J. Non-Crystalline Solids* 1998; **231**:17.
- [28] Manzini I, Antanioli G, Bersani D, Lottici P P, Gnappi G, and Montonero A, X-ray absorption spectroscopy study of crystallization processes in sol-gel-derived TiO₂. *J. Non-Cryst. Solids* 1995; **519**:192.
- [29] Chen E, Chang T. Walsh Diagram and the Linear Combination of Bond Orbital Method. *Journal of Molecular Structure: THEOCHEM* 1998; **431**: 127.
- [30] Robertson J. Physics of amorphous conducting oxides. *J. Non-Cryst. Solids* 2008; **354**, 2791.
- [31] Inam F, Lewis J P, Drabold D A. Hidden structures in amorphous solids. *Phys. Status Solidi A* 2010; **207**: 599.
- [32] Cai B, Drabold D A. Properties of amorphous GaN from first-principles simulations. *Phys. Rev. B* 2011; **84**: 075216.
- [33] Fedders P A, Drabold D A, Nakhmanson S. Theoretical study of band tail states in amorphous Si. *Phys. Rev. B*, 1998; **58**: 15624.
- [34] Valencia S, Marn J M, Restrepo G. Study of the bandgap of synthesized titanium dioxide nanoparticles using the sol-gel method and a hydrothermal treatment. *Open Mater. Sci.* 2010; **4**: 9.
- [35] Tang H, Berger H, Schmid P E, Levy F, Burri G. Photoluminescence in TiO₂ anatase single-crystals. *Solid State Communications* 1993; **87**:847–850.
- [36] Dong J J, Drabold D A. Atomistic structure of band tail states in amorphous silicon. *Phys. Rev. Lett.* 1998; **80**: 1928.
- [37] Loken C, Gruner D, Groer L, Peltier R, Bunn N et al. Scinet: Lessons learned from building a power-efficient top-20 system and data centre. *J. Phys.: Conf. Ser.* 2010; **256**:012026.